

## Study the erosion of Eurofer-97 steel with the linear plasma device GyM

Andrea Uccello<sup>a,\*</sup>, Francesco Ghezzi<sup>a</sup>, Janez Kovač<sup>b</sup>, Jernej Ekar<sup>b,c</sup>, Tatjana Filipič<sup>b</sup>, Iva Bogdanović Radović<sup>d</sup>, David Dellasega<sup>e</sup>, Vittoria Mellera<sup>a</sup>, Matteo Pedroni<sup>a</sup>, Daria Ricci<sup>a</sup>, GyM Team<sup>1</sup>

<sup>a</sup> Istituto per la Scienza e Tecnologia dei Plasmi, CNR, via Cozzi 53, 20125 Milan, Italy

<sup>b</sup> Jozef Stefan Institute, Jamova cesta 39, SI-1000 Ljubljana, Slovenia

<sup>c</sup> Jozef Stefan International Postgraduate School, Jamova cesta 39, SI-1000 Ljubljana, Slovenia

<sup>d</sup> Institut Ruđer Bošković, Bijenička cesta 54, 10000 Zagreb, Croatia

<sup>e</sup> Dipartimento di Energia, Politecnico di Milano, Via Ponzio 34/3, 20133 Milan, Italy

### ARTICLE INFO

#### Keywords:

Plasma facing components  
Eurofer-97 steel  
Erosion  
GyM  
Tokamak

### ABSTRACT

This work reports on the investigation of Eurofer-97 erosion behaviour when exposed to the deuterium plasma of the linear device GyM. The erosion dependence of Eurofer-97 on the deuterium ion fluence,  $\Phi \leq 2.3 \times 10^{25} \text{ m}^{-2}$ , and temperature of the samples,  $T = 600 \text{ K}$  and  $990 \text{ K}$ , was addressed. A bias voltage of  $-200 \text{ V}$  was applied to GyM sample holder during the experiments. Samples were deeply characterised by: profilometry, scanning electron microscopy, atomic force microscopy, energy-dispersive X-ray spectroscopy, time-of-flight secondary ion mass spectrometry, Rutherford backscattering spectroscopy and particle-induced X-ray emission.

The behaviour of Eurofer-97 erosion rate with the ion fluence strictly depends upon temperature. At  $600 \text{ K}$ , it was  $\sim 0.14 \text{ nm/s}$  after  $4.7 \times 10^{24} \text{ m}^{-2}$ , then decreased, reaching a steady state value of  $\sim 0.01 \text{ nm/s}$  from  $8.0 \times 10^{24} \text{ m}^{-2}$ . At  $990 \text{ K}$  instead, the erosion rate was roughly constant around  $0.019 \text{ nm/s}$  for  $\Phi \leq 1.24 \times 10^{25} \text{ m}^{-2}$ . The value at  $2.35 \times 10^{25} \text{ m}^{-2}$  was slightly lower. The erosion rate at  $990 \text{ K}$  was greater than that at  $600 \text{ K}$  for every ion fluence.

Microscopy and surface analysis techniques showed that Eurofer-97 erosion rate dependence on  $\Phi$  at  $600 \text{ K}$  was primarily determined by the preferential sputtering of iron and other mid-Z elements of the alloy, leading to a surface rich in W and Ta difficult to be sputtered. The erosion behaviour at  $990 \text{ K}$  was dominated by the morphology dynamics, instead. The different properties of the morphology developed at the two temperatures can explain the higher erosion rate at  $990 \text{ K}$  for all the ion fluences.

### 1. Introduction

The use of bare reduced activation ferritic martensitic (RAFM) steels, like Eurofer-97, has recently been envisaged as a possible option for the recessed elements of the first-wall of DEMO. The erosion by hydrogen isotope charge-exchange neutrals (CXNs), with the largest fluxes at low energies of up to  $200 \text{ eV}$ , can significantly affect the lifetime of these components and needs to be properly assessed [1]. RAFM steels are iron (Fe)-based alloys typically containing other mid-Z steel elements (e.g. chromium, Cr, manganese, Mn, vanadium, V) as well as small amounts of high-Z elements like tungsten, W, and tantalum, Ta ( $\sim 0.33 \text{ at.}\%$  W and  $\sim 0.04 \text{ at.}\%$  Ta for Eurofer-97). Being multi-component alloys, erosion of RAFM steels exposed to low energy hydrogen isotope ions may be influenced by:

- preferential sputtering of elements with high sputtering yield ( $Y$ ). In particular, since  $Y_{Fe} > Y_W$ , Fe erodes quickly, leading to a W-rich surface difficult to be sputtered [1–3];
- temperature-dependent processes, such as thermal diffusion and Gibbs segregation of the different components [4–11];
- surface morphology dynamics triggered by the interplay of particle bombardment and thermal effects [4,6,8–10,12,13].

This work reports on the investigation of Eurofer-97 erosion behaviour when exposed to the deuterium (D) plasma of the linear device GyM [14–17]. The ion flux of GyM of  $\Gamma = 10^{20}\text{--}10^{21} \text{ m}^{-2}\text{s}^{-1}$  is suitable to simulate the CXNs flux impinging on the recessed components of the DEMO first-wall [18]. Typical energies of D CXNs were obtained

\* Corresponding author.

E-mail address: [andrea.uccello@istp.cnr.it](mailto:andrea.uccello@istp.cnr.it) (A. Uccello).

<sup>1</sup> See Uccello et al. (2023) (<https://doi.org/10.3389/fphy.2023.1108175>) for the GyM Team.

applying a negative bias voltage to GyM sample holder. The erosion dependence of Eurofer-97 on the deuterium ion fluence,  $\Phi \leq 2.3 \times 10^{25} \text{ m}^{-2}$  and temperature of the samples,  $T = 600 \text{ K}$  and  $990 \text{ K}$ , was addressed.  $600 \text{ K}$  is inside Eurofer-97 allowable temperature boundaries of  $573 \text{ K}$  and  $823 \text{ K}$  (the lower and higher limits are determined by the ductile to brittle temperature transition and the potential for creep failure, respectively) [19].  $990 \text{ K}$  was chosen above the upper allowable  $T$  to investigate the effects of DEMO transient events.

Eurofer-97 samples were deeply characterised both before and after the exposure. The erosion rate was evaluated by profilometry. Scanning electron microscopy (SEM) and atomic force microscopy (AFM) were used to study the evolution of morphology and roughness of the samples. Compositional changes were investigated by means of energy-dispersive X-ray spectroscopy (EDXS), time-of-flight secondary ion mass spectrometry (ToF-SIMS), Rutherford backscattering spectroscopy (RBS) and particle-induced X-ray emission (PIXE).

This work adds to the broad literature of RAFM steels exposed to low energy deuterium ions of mass-selected ion beams [3,13] and plasmas of electron cyclotron resonance sources [6] and linear devices [1,4,8,10]. It continues the study of the sputtering properties of Fe-W coatings, model system of RAFM steels, with GyM [7].

With respect to most of the literature, the ion flux of the experiments presented here is very close to the predicted  $\Gamma_{CXN}$  reaching the remote regions of DEMO first-wall, as mentioned earlier. This is an important aspect, since both experiments [20] and modelling [5] have shown that the rate of erosion of pure metals and alloys by light ions may be flux-dependent. Moreover, emphasis is put on the comparison between, and linking of the results from the different characterisation techniques. In particular, SEM data are integrated with those from AFM to study the morphology evolution of Eurofer-97 samples from the micrometer to the nanoscale. An attempt to compare the main findings of the surface analysis techniques, having very different depth and lateral resolutions, is also presented. Finally, the information of morphology and compositional changes is combined with each other to explain the erosion behaviour of Eurofer-97 samples during deuterium plasma exposure.

Features of Eurofer-97 samples, the parameters of the exposures and the details of the characterisation techniques are described in Section 2. The results of the exposures and their interpretation are presented in Sections 3 and 4, respectively. Concluding remarks are given in Section 5.

## 2. Methods

Eurofer-97 RAFM steel has been developed in the European Union for fusion applications. It consists of Fe as the base material, Cr ( $\sim 9 \text{ at.}\%$ ), carbon, C ( $\sim 0.45 \text{ at.}\%$ ), Mn ( $\sim 0.4 \text{ at.}\%$ ), W ( $\sim 0.33 \text{ at.}\%$ ), V ( $\sim 0.2 \text{ at.}\%$ ), Ta ( $\sim 0.04 \text{ at.}\%$ ) and small amounts of other alloying elements [21].

Eight mirror finished  $10 \times 20 \times 1 \text{ mm}^3$  Eurofer-97 samples were exposed to the deuterium plasma of the linear device GyM [14–17]. The magnetic field configuration of the experiments is shown in Fig. 1a (the current flowing in the copper coils was  $600 \text{ A}$ ), together with the launching direction of the  $2.45 \text{ GHz}$  magnetron  $\mu$ -wave and the electron cyclotron resonance (ECR) layer at  $87.5 \text{ mT}$ . The working pressure and the magnetron power were  $4.0 \times 10^{-4} \text{ mbar}$  and  $1800 \text{ W}$ . These experimental conditions were chosen in order to maximise the deuterium ion flux, thus limiting as much as possible the plasma discharge duration required to reach the desired fluence. The D plasma parameters were measured with a cylindrical stainless steel Langmuir probe ( $10 \text{ mm}$  long and  $1.5 \text{ mm}$  in diameter) on the axis of GyM,  $\sim 30 \text{ cm}$  away from both the ECR layer and the sample holder (see Fig. 1a). The probe had its major axis perpendicular to the magnetic field lines. The plasma parameters remained approximately constant during all the experiments: the electron density and temperature were  $n_e = 5.0 \times 10^{16} \text{ m}^{-3}$  and  $T_e = 7 \text{ eV}$ , the plasma potential was  $V_{pl}$

$= 25 \text{ eV}$  and the deuterium ion flux was  $\Gamma = 4.0 \times 10^{20} \text{ m}^{-2}\text{s}^{-1}$ . A heatable and biasable stainless steel manipulator with a molybdenum (Mo) sample cover ( $1 \text{ mm}$  thick) was used [7,16,17] (see Fig. 1b). The latter allowed the exposure of 2 samples at a time (Fig. 1c–d). The surface of the samples was perpendicular to the magnetic field lines and pointed toward the ECR layer. The centre of the Mo cover was on the axis of GyM. The temperature of the carrier head was measured by an Inconel sheathed type K thermocouple with the hot junction near the target holder.

The Eurofer-97 specimens were exposed at  $600 \text{ K}$  and  $990 \text{ K}$  and four different ion fluences in the range  $4.6 \times 10^{24}$ – $2.35 \times 10^{25} \text{ m}^{-2}$ . The deuterium species mix of the plasma of GyM is not available at the moment.  $\Phi$  is thus equal to  $\Phi_{D^+} + \Phi_{D_2^+} + \Phi_{D_3^+}$ , here. A bias voltage of  $-200 \text{ V}$  was applied to the sample holder. As a result, the energy per ion was  $E_{ion} = 200 \text{ eV} + V_{pl} = 225 \text{ eV}$ . Since the erosion of W (and Ta) by  $D^+$  is almost negligible at this energy (W sputtering threshold energy is  $216 \text{ eV}$  [22]),  $-200 \text{ V}$  allowed in principle to enhance preferential sputtering of Fe and the other mid-Z elements of Eurofer-97 (Cr, Mn and V). Incident deuterium molecular ions also contributed to mid-Z elements selective erosion.  $D_2^+$  and  $D_3^+$  resulted in  $1/2$  and  $1/3$  of  $E_{ion}$  after breakup of the molecules [1]. From [22] and  $E_{ion} = 225 \text{ eV}$ ,  $Y_{Fe}(E_{ion}/2)$  and  $Y_{Fe}(E_{ion}/3)$  are  $\sim 0.4$  and  $\sim 0.15$  times  $Y_{Fe}(E_{ion})$ . The sputtering contribution of  $D_2^+$  and  $D_3^+$  was thus  $\sim 0.8$  and  $\sim 0.45$  that of  $D^+$ . Furthermore, plasma impurities may have had a role in the erosion of Eurofer-97 samples. Carbon, nitrogen (N) and oxygen (O) impurities could reach the plasma being ejected from the electrically grounded wall of GyM as a consequence of thermal desorption. The sample holder stainless steel carrier head, the cover and the strip for profilometry, all biased at  $-200 \text{ V}$ , were other sources of these impurities, together with sputtered Fe and Mo atoms. Neutral impurities should be ionised to sputter the Eurofer-97 samples. However, due to the fairly low GyM plasma density, the values of the mean free path (MFP) for the different ionisation reactions are of the same order of magnitude of or greater than the characteristic dimensions of the device (which is  $2.11 \text{ m}$  long and  $0.25 \text{ m}$  in diameter [17]). In particular, the MFPs for electron impact ionisation of sputtered Fe and Mo atoms (for  $n_e = 5.0 \times 10^{16} \text{ m}^{-3}$  and  $T_e = 7 \text{ eV}$ ) are  $>1 \text{ m}$  and  $\sim 0.4 \text{ m}$ . Since  $D^+$  energy was in the range of hundreds of eV, the MFPs have been estimated considering the Thompson–Sigmund energy distribution function with  $\alpha = 5$  for the sputtered particles to take account of the energy distribution shrinkage and peak shift to lower energies in comparison to the classical Thompson distribution, more valid for higher incidence ion energies [23]. Moreover, the MFP for electron impact ionisation of thermal desorbed species is of the same order of magnitude of the GyM length, e.g.  $\sim 3 \text{ m}$  for  $N_2$ . All these neutral impurities had therefore a great chance to be deposited on the wall of GyM again before being ionised. For this reason, their contribution to the sputtering of Eurofer-97 samples should have been low.

For each temperature, three exposures of  $3 \text{ h}$ ,  $5 \text{ h}$  and  $7 \text{ h}$ , were done. Two Eurofer-97 samples were exposed every time (see Fig. 1b–d). At the end of each exposure, only one specimen was replaced. The other one was left in place. This allowed to obtain the highest investigated ion fluence of  $2.35 \times 10^{25} \text{ m}^{-2}$ , corresponding to  $15 \text{ h}$  of D plasma.

Before the plasma exposure, each Eurofer-97 sample was partially masked by a Mo strip ( $0.1 \text{ mm}$  thick, Fig. 1c) to evaluate, after the experiment, the erosion of the specimen by means of a KLA Tenchro mechanical profilometer (resolution of some nm), measuring the erosion step height between the exposed and the covered side. Twenty-one independent chords,  $2 \text{ mm}$  long and  $\sim 0.25 \text{ mm}$  spaced, were taken at different positions along the middle part of the trace left by the Mo foil (see Fig. 1d). The step was at the centre of each chord. The average value and standard deviation of the step were calculated.

The topography of the samples was investigated by a Nano-R™ AFM in air (Pacific Nanotechnology, Santa Clara, CA, USA). A first set of images was taken in contact mode on an area of  $30 \times 30 \mu\text{m}^2$ , at a scan speed of  $43 \mu\text{m}\cdot\text{s}^{-1}$  and with 256 imaged points per scanned line.

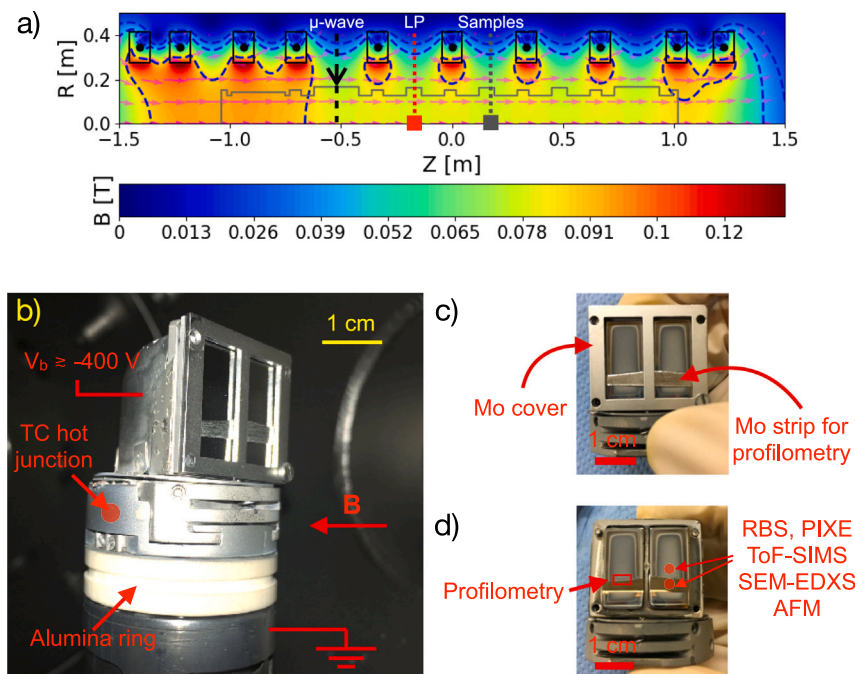


**Fig. 1.** Magnetic field configuration of GyM (a). The dashed black arrow indicates the launching direction of the 2.45 GHz magnetron  $\mu$ -wave. The blue dashed lines represent the magnetic field required for ECR at 2.45 GHz: 87.5 mT. The locations of Langmuir probe (LP) and the sample holder are also reported. Photographs of: the hot manipulator (b), the sample holder w/ (c) and w/o (d) the Mo cover and strip for profilometry. Figure (b) also displays the positions of the K thermocouple hot junction and of the alumina ring which electrically insulates the biased sample holder from the grounded manipulator [16,17]. Figure (d) shows the approximate location of the measurement spots on the sample of the different characterisation techniques. (For interpretation of the references to colour in this figure legend, the reader is referred to the web version of this article.)

For each sample, two  $30 \times 30 \mu\text{m}^2$  AFM topography images of nearby regions were acquired. A second set of images was taken in tapping mode on an area of  $10 \times 10 \mu\text{m}^2$ , at a scan speed of  $4.8 \mu\text{m}\cdot\text{s}^{-1}$ , keeping the number of points per line unchanged. For each sample, only one  $10 \times 10 \mu\text{m}^2$  AFM topography image was acquired. A Zeiss Supra 40 field emission SEM (accelerating voltage 5–10 kV) was used to study the evolution of the morphology of the specimens.

W and Ta enrichment of the surface of Eurofer-97 samples was evaluated by RBS. The measurements were performed using a 3 MeV  $\text{Li}^{3+}$  beam, with normal incidence toward the sample's surface. The ion beam was collimated through a diameter of 3 mm. The RBS detector was placed at  $165^\circ$  angle toward the beam direction. Simultaneously, PIXE spectra were collected using a silicon drift detector at  $150^\circ$  to identify possible Mo contamination from the sample holder. The depth resolution of the RBS setup was  $\sim 20$  nm. The uncertainty of the measurements was  $\sim 8\%$  and was mainly due to the uncertainty in peak statistics and charge collection. Spectra analysis was done using the simulation code SIMNRA [24,25]. For both RBS and PIXE, W and Ta peaks could not be resolved and these elements are treated together in the following.

Compositional changes of the surface of the samples were also evaluated by ToF-SIMS. The analyses were performed using a ToF-SIMS 5 instrument (ION-TOF, Münster, Germany) equipped with a bismuth (Bi) liquid metal ion gun with a kinetic energy of 30 KeV. The SIMS spectra were measured by scanning the  $\text{Bi}^+$  ion beam over an area of  $0.1 \times 0.1 \text{ mm}^2$ . SIMS depth profiles were performed in dual beam depth profiling mode using a 2 KeV cesium ion  $\text{Cs}^+$  beam, rastering over  $0.4 \times 0.4 \text{ mm}^2$  for sputtering, and the  $\text{Bi}^+$  beam for analysis [26]. Etching rate was estimated to be 0.2 nm/s. In order to compare SIMS results, all the profiles were measured in the same way. The profile acquisition was stopped after 600 s. Considering the aforementioned sputtering rate of  $\sim 0.2$  nm/s, a depth of about 120 nm was analysed on all the specimens. During depth profile measurements, oxygen gas was introduced in the analyses chamber at a pressure of  $5.0 \times 10^{-7}$  mbar in order to slightly oxidise the surface, thus increasing

the ionisation probability and the detection efficiency of secondary ions. Negative secondary ions emitted from the surface of the samples under bombardment of the  $\text{Bi}^+$  ion beam were acquired (beam current 1 pA). The samples exposed at  $1.10 \times 10^{25} \text{ m}^{-2}$  were measured in two places to estimate results uncertainty. The latter was found to be  $\sim 5\%$  and was mainly due to heterogeneity of the specimens.

Modifications of the (metal elements) composition of the surface of Eurofer-97 samples at micrometer-scale and below were measured by EDX in SEM with lateral resolution of tens of nanometers. The analyses were performed on a JSM-7600F field emission scanning microscope (JEOL company, Tokyo, Japan). EDX spectra were measured with INCA Oxford 350 EDS spectrometer in the energy range 0–10 KeV using a primary electron beam of 15 KeV to provide some surface sensitivity. The downside of this was a low signal at 8 KeV for the detection of the well-separated L-lines of W and Ta (8.396 KeV and 8.145 KeV for W and Ta  $L\alpha$ , respectively). The contributions from these two elements were instead evaluated by measuring W and Ta M-lines around 1.7 KeV, whose distance was below the energy resolution of the EDXS detector. W and Ta from EDXS will be therefore considered together in the paper.

Microscopic and compositional analyses were done both at the plasma exposed region and at the protected region under the Mo strip (see Fig. 1d), to separate the thermal effects in deuterium atmosphere ( $4.0 \times 10^{-4}$  mbar) from those of the plasma particle load.

### 3. Results

This section presents the results of Eurofer-97 samples analysis by the different characterisation techniques considered in this work. The morphology and topography evolution of the samples during the exposures, investigated with SEM and AFM, is shown in Section 3.1. The compositional changes measured by RBS, PIXE, ToF-SIMS and EDXS are described in Section 3.2. Finally, the erosion rate of the samples from profilometry is reported in Section 3.3.

The interpretation of the results here presented and their comparison with the available literature are left to the Discussion Section 4.



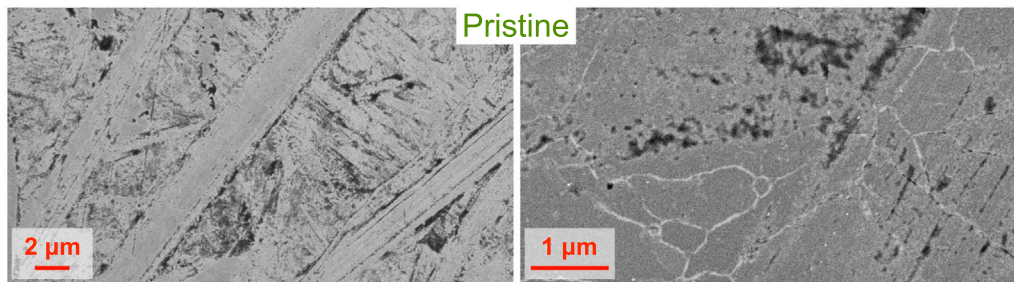


Fig. 2. SEM top-view images of the virgin Eurofer-97 sample at two magnifications, in left (10 kX) and right (50 kX) panels.

### 3.1. Morphology and topography evolution

The effects of the exposures on the morphology of the Eurofer-97 samples were investigated by SEM. Fig. 2 shows the SEM top-view images of the surface of a pristine specimen. Figs. 3a–d and 4a–d show the SEM top-view images of the surface of the samples after the exposure to different deuterium ion fluences at 600 K and 990 K, respectively. Figures (e) display the surface below the Mo strip after the exposures at the highest  $\Phi$ . SEM images are given at two magnifications in the left and right panels of Figs. 2, 3 and 4. The difference between virgin and exposed surfaces is significant at every ion fluence, for both the temperatures. The formation of a “fence/corral”-like (FC) morphology [8] on the exposed region of the samples can be clearly seen from Figs. 3a–d and 4a–d. SEM images (e) show that this did not occur below the strip for profilometry, instead. In fact, the protected region was only affected by the deposition of contaminants. The development of the FC morphology was therefore triggered by the interaction of the samples with the deuterium plasma and cannot be solely ascribed to thermal effects.

Temperature  $T$  of the samples during the exposure had a great impact on the morphology evolution. The properties of the FC morphology discussed in the following are: coverage of the surface, nanostructure surface density and size (lateral length and height). In particular, we evaluate the coverage from SEM low-magnification images, to understand to what extent the FC morphology developed at the micrometer-scale. Full coverage is reached when the distance between two adjacent nanostructures is  $\lesssim 1 \mu\text{m}$ . In addition, we define the nanostructure surface density as the ratio of the projected area of the nanostructures to the area of SEM high-magnification micrographs. It was estimated by thresholding the SEM images using ImageJ software [27]. At 600 K, the FC morphology formed even at the lowest  $\Phi$  (Fig. 3a–d). SEM low-magnification images (left column) of the surface of the samples exposed at  $4.7 \times 10^{24} \text{ m}^{-2}$  and  $7.8 \times 10^{24} \text{ m}^{-2}$  show that the dendrite growth dynamics is grain-dependent [13]. The FC morphology becomes homogeneous at higher ion fluences. At 990 K and  $4.6 \times 10^{24} \text{ m}^{-2}$ , the surface looks damaged (Fig. 4a). First nanostructures begin to see from  $\Phi = 7.8 \times 10^{24} \text{ m}^{-2}$  (Fig. 4b, left panel). Almost full coverage of the surface was obtained at the lowest and the highest ion fluence for  $T = 600 \text{ K}$  and  $990 \text{ K}$ , respectively. At high SEM magnification, a higher degree of connection among the dendrites is evident at 600 K increasing  $\Phi$  (right column of Fig. 3a–d). At 990 K, nanostructures not only coalesced each other but also grew in lateral length (right column of Fig. 4c–d). Comparing the SEM micrographs of the exposed regions at the highest  $\Phi$  (Figs. 3d and 4d), one can observe that the surface density of the FC morphology is (a factor  $\sim 2$ ) higher at 600 K than at 990 K but the lateral length of the dendrites is (a factor  $\sim 3$ ) lower. Finally, SEM  $45^\circ$  tilted images of Fig. 5 show that the height of the nanostructures is a few tens of nm at 600 K and hundreds of nm at 990 K.

Both  $30 \times 30 \mu\text{m}^2$  and  $10 \times 10 \mu\text{m}^2$  AFM images of Eurofer-97 samples were taken to investigate the surface inhomogeneities on the one hand and the features of the FC morphology on the other hand. The AFM results on a scan area of  $30 \times 30 \mu\text{m}^2$  are reported in Fig. 6. It

shows the behaviour of the root mean square (RMS) roughness of the specimens increasing  $\Phi$  (a) and the topography images of the surface of a pristine sample (b) and after exposure at 600 K (c, e, g) and 990 K (d, f, h), for three different fluences. The data point at  $\Phi = 0 \text{ m}^{-2}$  of Fig. 6a represents the RMS roughness of the virgin specimens.

Fig. 7 shows the  $10 \times 10 \mu\text{m}^2$  AFM images of the surface of the same samples of Fig. 6c–h. Image 7f of the specimen exposed at 990 K and  $1.10 \times 10^{25} \text{ m}^{-2}$  was acquired in a region where the FC morphology developed. The AFM tip had a conical shape, a radius of 10 nm and a sidewall angle of  $10^\circ$ . It could properly reflect the features of Eurofer-97 surface after the experiments. Indeed, if one considers the sample exposed at 600 K for the highest  $\Phi$  as a limit example, its high-magnification SEM image (Fig. 3d, right column) shows that the distance between two adjacent dendrites is  $>50 \text{ nm}$ , on average. The AFM tip could penetrate  $\sim 90 \text{ nm}$  in depth among features spaced 50 nm apart. This value is well above the dendrites' height of roughly a few tens of nanometers as estimated from the SEM tilted image of Fig. 5a.

Surface nanostructures of the samples exposed at 600 K are clear from  $10 \times 10 \mu\text{m}^2$  AFM images (Fig. 7c, e, g). They can hardly be seen in the  $30 \times 30 \mu\text{m}^2$  AFM images (Fig. 6c, e, g), instead. This is due to the small dendrites' lateral length of 100–200 nm (see SEM micrographs 3a–d) combined with a limited number of sampling points. Nevertheless, RMS roughnesses of  $10 \times 10 \mu\text{m}^2$  and  $30 \times 30 \mu\text{m}^2$  micrographs of the same specimen are very similar as a consequence of the homogeneous nanostructuring of the surface at 600 K (RMS roughness values are reported in Fig. 6a and in the lower-right part of AFM images of both Figs. 6 and 7).  $30 \times 30 \mu\text{m}^2$  micrographs confirm that the growth dynamics of the FC morphology is grain-dependent, as shown by SEM images 3a–b of the samples exposed at  $4.7 \times 10^{24} \text{ m}^{-2}$  and  $7.8 \times 10^{24} \text{ m}^{-2}$ . The higher AFM vertical resolution allows to detect the grain boundaries even at the other ion fluence values. The high lateral length of the FC morphology developed at 990 K makes them visible in the  $30 \times 30 \mu\text{m}^2$  AFM images of the samples exposed at  $\Phi \geq 1.10 \times 10^{25} \text{ m}^{-2}$  (Fig. 6f,h), as well. In addition, islands in which nanostructures developed (e.g. the one inside the white line) separated by low-roughness regions (e.g. the one inside the black line) are evident from image 6f, in agreement with SEM Fig. 4c, left column. This pronounced non-uniform nanostructuring at 990 K and  $1.10 \times 10^{25} \text{ m}^{-2}$  is the reason of the big difference between RMS roughness values of  $30 \times 30 \mu\text{m}^2$  and  $10 \times 10 \mu\text{m}^2$  micrographs 6f and 7f.

The RMS roughness of the specimens exposed at 600 K is constant at  $\sim 30 \text{ nm}$  with increasing  $\Phi$  and the nanostructures are rather similar in density and size ( $10 \times 10 \mu\text{m}^2$  AFM images 7c, e, g). Instead, the RMS roughness of  $30 \times 30 \mu\text{m}^2$  micrographs (Fig. 6a) linearly increases with the ion fluence up to  $\sim 220 \text{ nm}$  at the highest  $\Phi$  for the samples exposed at 990 K. This is due to the increase of both the coverage of the surface by and the height of the nanostructures, as shown by  $30 \times 30 \mu\text{m}^2$  and  $10 \times 10 \mu\text{m}^2$  AFM images (Figs. 6d, f, h and 7d, f, h), respectively. Moreover, by comparing  $10 \times 10 \mu\text{m}^2$  micrographs of samples exposed at the same  $\Phi \geq 1.10 \times 10^{25} \text{ m}^{-2}$ , one can see that both the lateral length and height of the nanostructures are higher at the highest  $T$ .

AFM and SEM analyses are in agreement with each other. Indeed, AFM images and RMS roughness behaviour with  $\Phi$  confirm that: (i) a



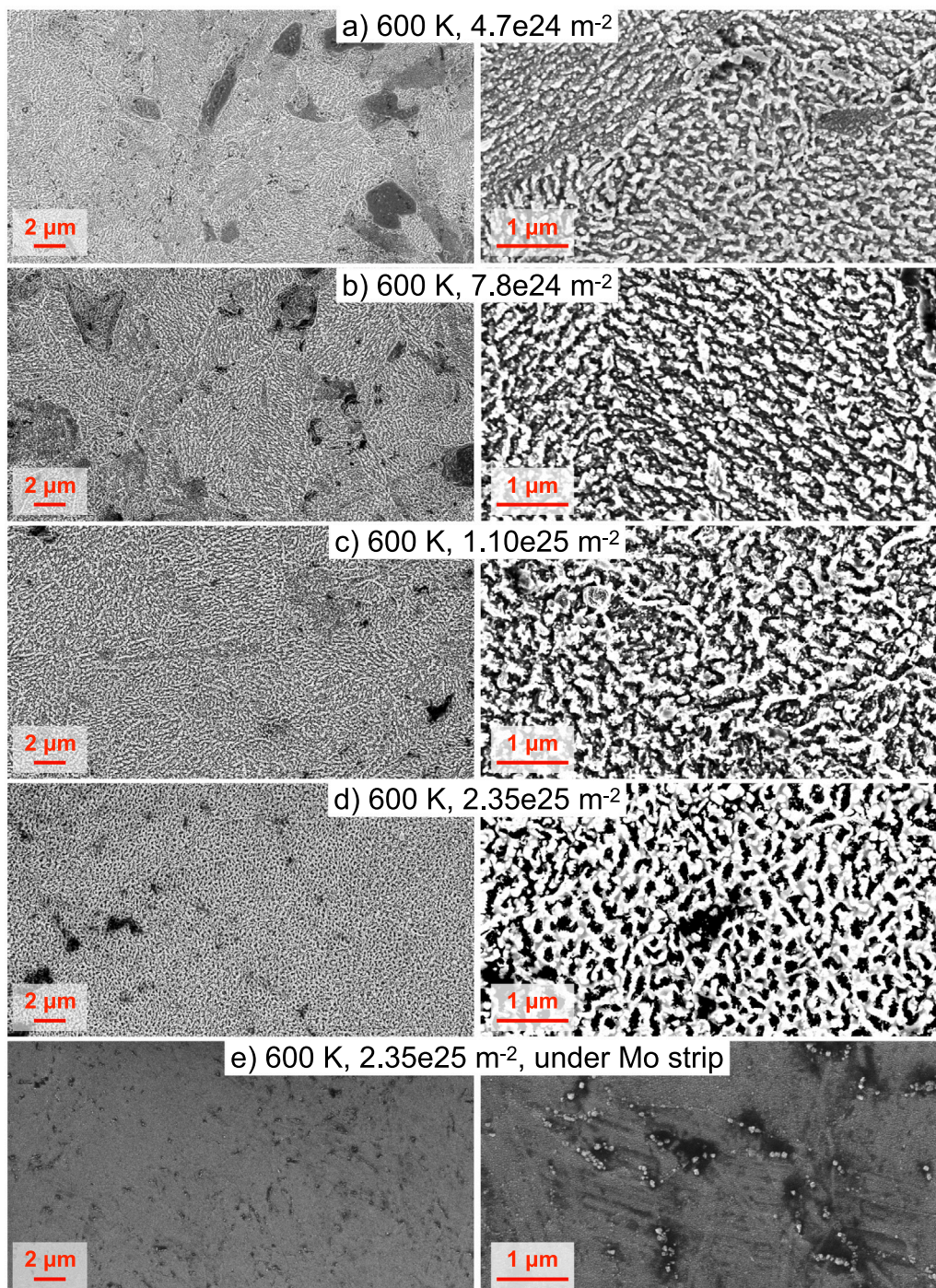


**Fig. 3.** (a–d) SEM top-view images of Eurofer-97 samples after exposure at 600 K, for different fluences. (e) SEM top-view images of the region covered by the Mo strip at 600 K, for the highest  $\Phi$  (e). SEM images are given at two magnifications in left (10 kX) and right (50 kX) columns.

significant change of the surface of Eurofer-97 samples occurred even for the lowest ion fluence at both the temperatures, (ii) the surface dynamics clearly depends on T, (iii) the FC morphology at 600 K reached a quasi steady state from the lowest value of  $\Phi$ , while it was evolving by increasing the ion fluence at 990 K and (iv) the size of the nanostructures is larger at 990 K.

### 3.2. Compositional changes

Fig. 8 shows the RBS spectra of the Eurofer-97 samples exposed at 600 K (a) and 990 K (b), together with that of the pristine specimen.

Some spectra show a peak from W+Ta at  $\sim 2600$  KeV. The edge at  $\sim 1900$  KeV comes from Fe and Cr. The signal at  $\sim 2250$  KeV of the specimens exposed at the highest fluences is likely due to the Mo contamination from the sample holder (Fig. 1c). The presence of Mo on the surface of the samples at the end of the experiments is further confirmed by the PIXE spectra of the specimens exposed at  $2.35 \times 10^{25} \text{ m}^{-2}$ , which show the peak at 2.29 KeV of the Mo L $\alpha$  X-ray line (Fig. 9). This feature is absent in the spectrum of the virgin sample, instead.

The amount of W+Ta and Mo, in terms of areal density, on the surface of the Eurofer-97 samples was quantified from the RBS spectra of Fig. 8 using the simulation code SIMNRA [24,25]. It is reported,



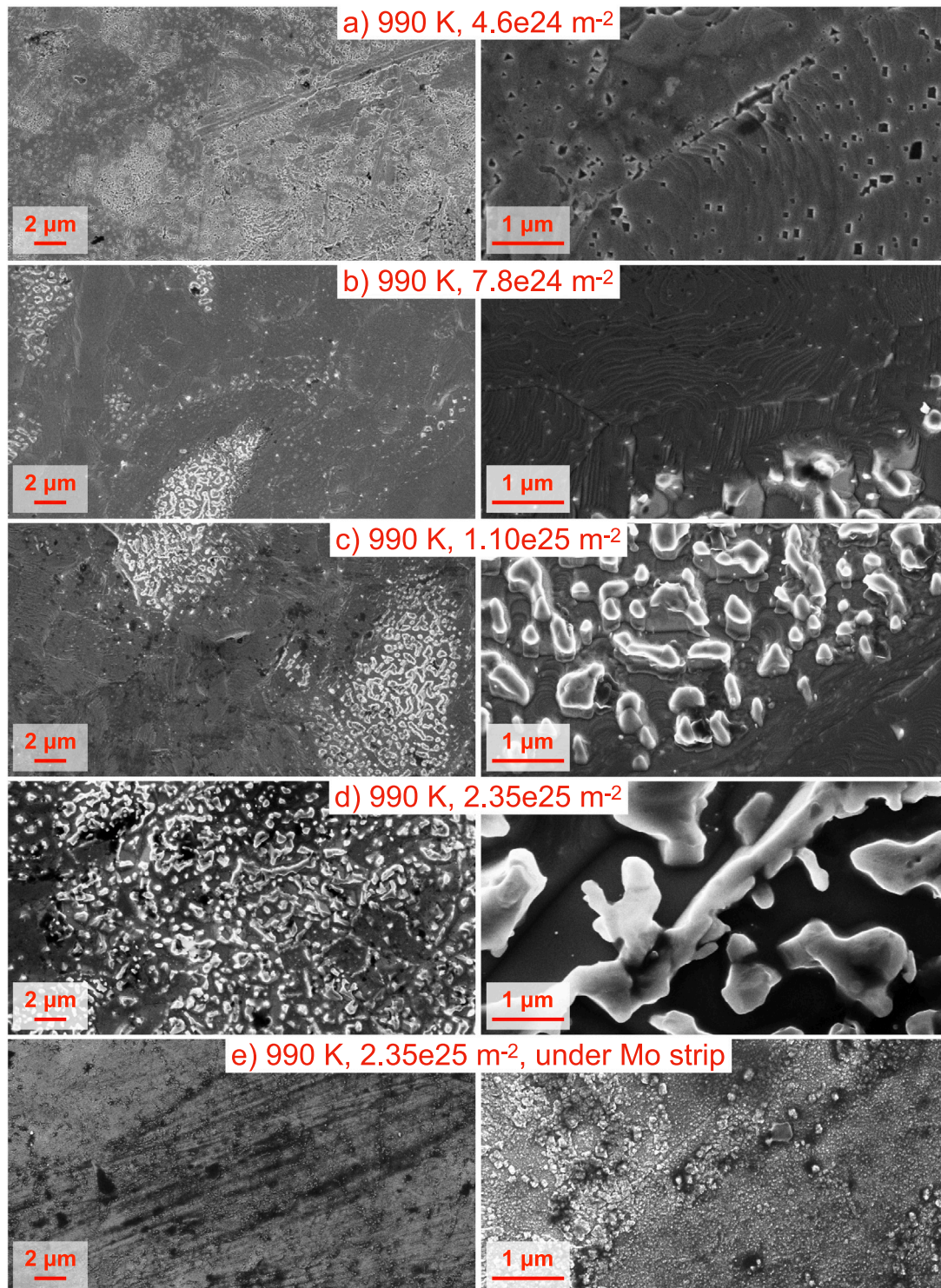


Fig. 4. (a–d) SEM top-view images of Eurofer-97 samples after exposure at 990 K, for different fluences. (e) SEM top-view images of the region covered by the Mo strip at 990 K, for the highest  $\Phi$  (e). SEM images are given at two magnifications in left (10 kX) and right (50 kX) columns.

as a function of  $\Phi$ , for the two temperatures, in Fig. 10a. For the pristine specimens, the amount of W+Ta and Mo is negligible (data points at  $\Phi = 0 \text{ m}^{-2}$ ). Considering the exposed samples, the W+Ta areal density at 600 K initially increases with the ion fluence before reaching a steady state from  $1.0 \times 10^{25} \text{ m}^{-2}$ . At 990 K, the amount of W+Ta depends quasi-linearly on  $\Phi$ . Moreover, the W+Ta areal density is lower at 990 K, except for the highest fluence here investigated. Same considerations can be drawn as far as Mo areal density is concerned,

whose range of values is really close to that of W+Ta areal density. The deposition of Mo on Eurofer-97 samples during the experiments thus cannot be overlooked and needs to be taken carefully into account in the interpretation of the results.

For each sample, the same analysis was repeated at the region protected by the Mo strip during the experiment. The two main findings are: (i) W+Ta areal density is negligible for all the specimens, even for those exposed at 990 K, (ii) considering the samples exposed at the

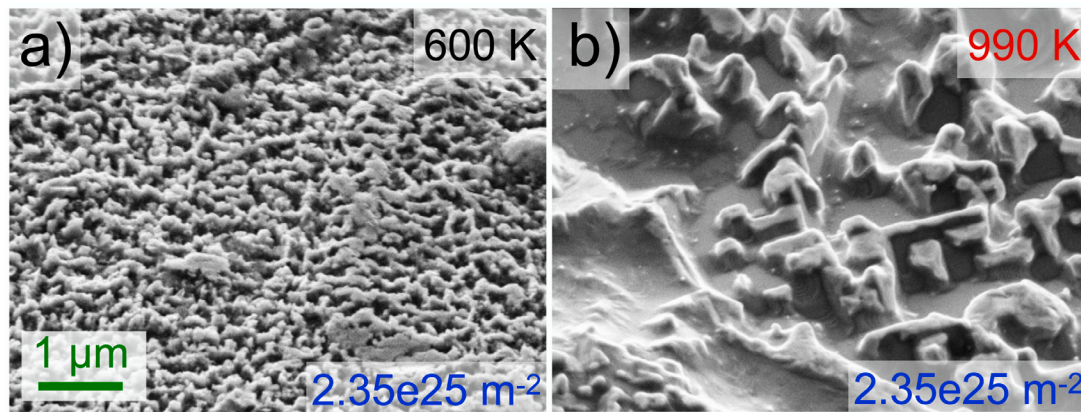


Fig. 5. SEM 45° tilted images of the Eurofer-97 samples exposed at 600 K (a) and 990 K (b), for the highest ion fluence.

higher fluences, Mo contamination is heavier (up to  $2.0 \times 10^{16}$  at.cm $^{-2}$ ) than the one measured at the plasma wetted region.

Compositional changes of the surface and subsurface regions of Eurofer-97 samples were also studied with ToF-SIMS depth profiling. Fig. 10b shows the integrated signals of WO $^{-}$  and MoO $^{-}$  during sputtering by the 2 KeV Cs $^{+}$  beam as a function of deuterium plasma fluence, for the two temperatures. As mentioned in Section 2, the results present the amount of detected ions over a depth region of  $\sim 120$  nm. WO $^{-}$  and MoO $^{-}$  integrated signals are almost negligible for the pristine specimens (data points at  $\Phi = 0$  m $^{-2}$ ). By comparing Figs. 10a and b, one can see that RBS and SIMS results are qualitatively consistent with each other, in spite of the different investigated area (7 mm $^2$  for RBS against  $10^{-2}$  mm $^2$  for SIMS) and depth ( $\sim 1$   $\mu$ m for RBS against  $\sim 120$  nm for SIMS). Indeed, integrated signals from WO $^{-}$  at 600 K increase rapidly with the ion fluence for  $\Phi \leq 1.10 \times 10^{25}$  m $^{-2}$ . At 990 K, they are quasi-linear with  $\Phi$ . W amount is lower at 990 K in general, but the trend reverses at the highest  $\Phi$ . Moreover, MoO $^{-}$  and WO $^{-}$  integrated signals almost show the same behaviour with both  $\Phi$  and T. The main differences among RBS and SIMS results concern Mo contamination. (i) At 990 K and  $4.6 \times 10^{24}$  m $^{-2}$ , SIMS measured a high MoO $^{-}$  integrated signal while the Mo areal density from RBS was negligible. (ii) At  $2.35 \times 10^{25}$  m $^{-2}$ , Mo amount is higher at 990 K than at 600 K for SIMS and vice versa for RBS (and PIXE, see Fig. 9). An inhomogeneous distribution of Mo contamination on the surface of the exposed samples combined with the different area and depth probed by the two characterisation techniques may be a plausible explanation for such discrepancies.

As regards the region protected by the Mo strip, ToF-SIMS depth profiles confirm RBS results again: WO $^{-}$  signals are negligible for all the samples and Mo contamination is always present. In addition, ToF-SIMS indicates a significant increase of Ta and mid-Z elements other than Fe (i.e. Cr, Mn and V).

Finally, EDXS was used to investigate modifications of Eurofer-97 sample (metal elements) composition at the micrometer-scale and below. Fig. 11 shows the results of a 2.7  $\mu$ m line-scan analysis over a nanostructure of the specimen exposed at the highest fluence and 990 K. Nanostructures are enriched by W+Ta and Mo while depleted of Fe and Cr. The situation is reversed on the flat surface.

### 3.3. Erosion rate

Fig. 12 shows the erosion rate of Eurofer-97 samples as a function of the ion fluence, for 600 K and 990 K. Each scatter point is the average of the twenty-one independent profilometry measurements of the eroded step of one specimen divided by the exposure time. The error bar represents the associated standard deviation. The points at  $1.24 \times 10^{25}$  m $^{-2}$ , i.e. 8 h of D plasma, refer to the samples cumulatively exposed for 15 h that were removed from the sample-holder after the first two

experiments, lasting 3 h and 5 h, for profilometry measurements. The behaviour of the erosion rate with  $\Phi$  strictly depends upon T. At 600 K, it initially decreases, reaching then a steady state value of  $\sim 0.01$  nm/s from  $8.0 \times 10^{24}$  m $^{-2}$ . At 990 K instead, the erosion rate is roughly constant around 0.019 nm/s for  $\Phi \leq 1.24 \times 10^{25}$  m $^{-2}$ . The value at  $2.35 \times 10^{25}$  m $^{-2}$  is slightly lower. The erosion rate at 990 K is greater than that at 600 K for every ion fluence.

## 4. Discussion

In this work, Eurofer-97 samples were exposed to the deuterium plasma of GyM at T of 600 K and 990 K,  $\Phi$  in the range  $4.6 \times 10^{24}$ – $2.35 \times 10^{25}$  m $^{-2}$  and  $E_{ion}$  of  $\sim 225$  eV. Mo contamination from the sample holder was found on top of all the specimens at the end of the experiments.

Rough micro-structured layers can be seen on the surface of the samples at the end of all the experiments by SEM (Figs. 3, 4 and 5) and AFM (Figs. 6 and 7). The morphology depends on both the ion fluence and sample temperature. In particular, an enhancement of the formation of surface roughness and an increase of the lateral length scale are observed raising the temperature. Moreover, EDXS (Fig. 11) shows that surface nanostructures are enriched by W(+Ta) (and Mo). All of these findings are consistent with the literature of RAFM steels exposed to low energy (up to a few hundred eV) deuterium ions [4,6,8,10,13]. At a closer look, Eurofer-97 samples exposed in GyM developed a morphology very similar to the fence/corral-like one shown in [8], although the fluence was much higher ( $10^{26}$ – $10^{27}$  m $^{-2}$ ) and the ion energy was lower ( $\sim 40$  eV), there. In [8], changing the ion fluence from  $2 \times 10^{26}$  m $^{-2}$  to  $10^{27}$  m $^{-2}$  did not lead to a different morphology, neither in type nor in length scale. As a consequence of the lower values of  $\Phi$  investigated here, morphology evolution was still ongoing at the higher ion fluences. This is especially the case of the exposures at 990 K: nanostructures were still coalescing and growing in lateral length (Fig. 4c–d, right column).

The other remarkable difference with [8] is the temperature required for the formation of the FC morphology with a given lateral length. First, the minimum temperature at which the FC morphology was observed is:  $< 600$  K in the present work and  $> 770$  K in [8]. Second, dendrites' lateral length of the samples exposed at 600 K in GyM (Fig. 3d) is close to the one obtained at 870 K in [8] (figure 3 g of [8]). These discrepancies could be partly explained by the different deuterium ion energy of the two experiments. Indeed, one of the processes contributing to RAFM steels' morphology development is the preferential sputtering of mid-Z elements (Fe, Cr, etc.), which significantly depends on  $E_{ion}$  [4,6,8,10].

The formation of the FC morphology with W(+Ta) and Mo enriched nanostructures on the surface of the Eurofer-97 samples exposed to the deuterium plasma of GyM can be attributed to the synergistic



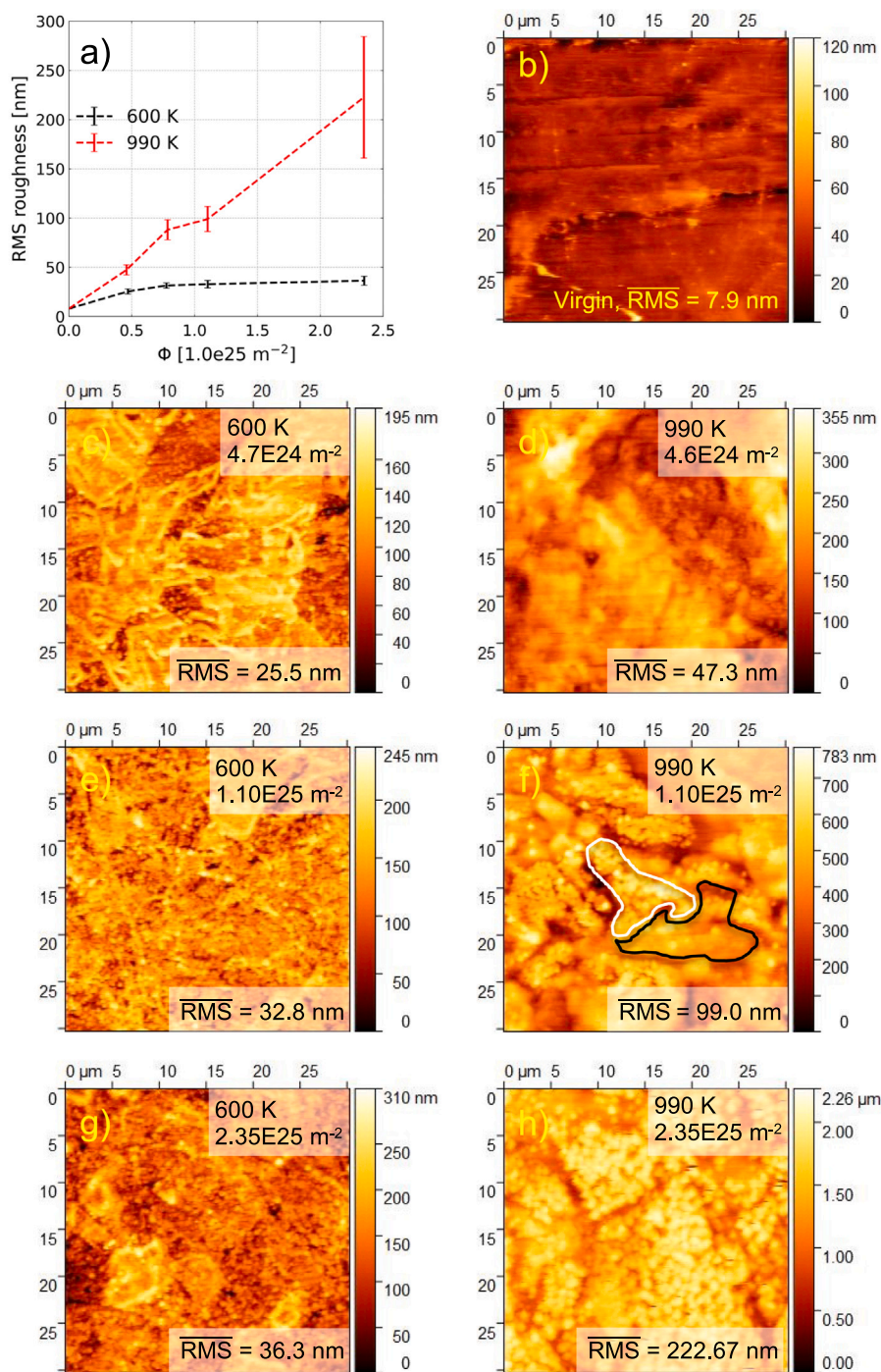


**Fig. 6.** AFM results on a scan area of  $30 \times 30 \mu\text{m}^2$ . (a) Root mean square (RMS) roughness as a function of the ion fluence at 600 K (in black) and 990 K (in red). The data point at  $\Phi = 0 \text{ m}^{-2}$  represents the RMS roughness of the virgin specimens. Each scatter point is the average among the RMS roughness values of two different AFM topography images of the same sample and the error bar represents the associated standard deviation. Dashed lines are drawn to guide the eye. (b) AFM image of a pristine Eurofer-97 specimen. (c–h) AFM images of the samples exposed at 600 K (c, e, g) and 990 K (d, f, h), for three different fluences. The white and black lines of image (f) delimit one of the islands in which nanostructures developed and one of the low-roughness regions, respectively. (For interpretation of the references to colour in this figure legend, the reader is referred to the web version of this article.)

effect of a multitude of processes [4,6,8,10]: the aforementioned preferential sputtering of mid-Z elements, the radiation-induced surface segregation, the radiation-enhanced diffusion, the deuterium-enhanced surface diffusion, the “simple” thermal surface diffusion and the nanocrystallite nucleation induced by high-Z elements, like W and Ta of the alloy but also deposited Mo. Gibbsian segregation (GS) of W can be ruled out since its areal density from RBS and the  $\text{WO}^-$  signal from ToF-SIMS are negligible in the region protected by the Mo strip (as it is

for the pristine samples), at both the temperatures. The signal of  $\text{TaO}^-$  increased, instead (this was also the case of  $\text{CrO}^-$ ,  $\text{MnO}^-$ ,  $\text{VO}_2^-$ ). GS of Ta (Cr, Mn and V) thus probably occurred but its atomic ratio in the Eurofer-97 bulk is about one order of magnitude lower than that of W.

As reported in Section 3.1, the SEM analysis is in agreement with AFM results. It was also pointed out that W(+Ta) and Mo enriched FC morphology did not significantly change with the ion fluence at 600 K (Figs. 3a–d and 7c, e, g), while nanostructures’ size (lateral length and



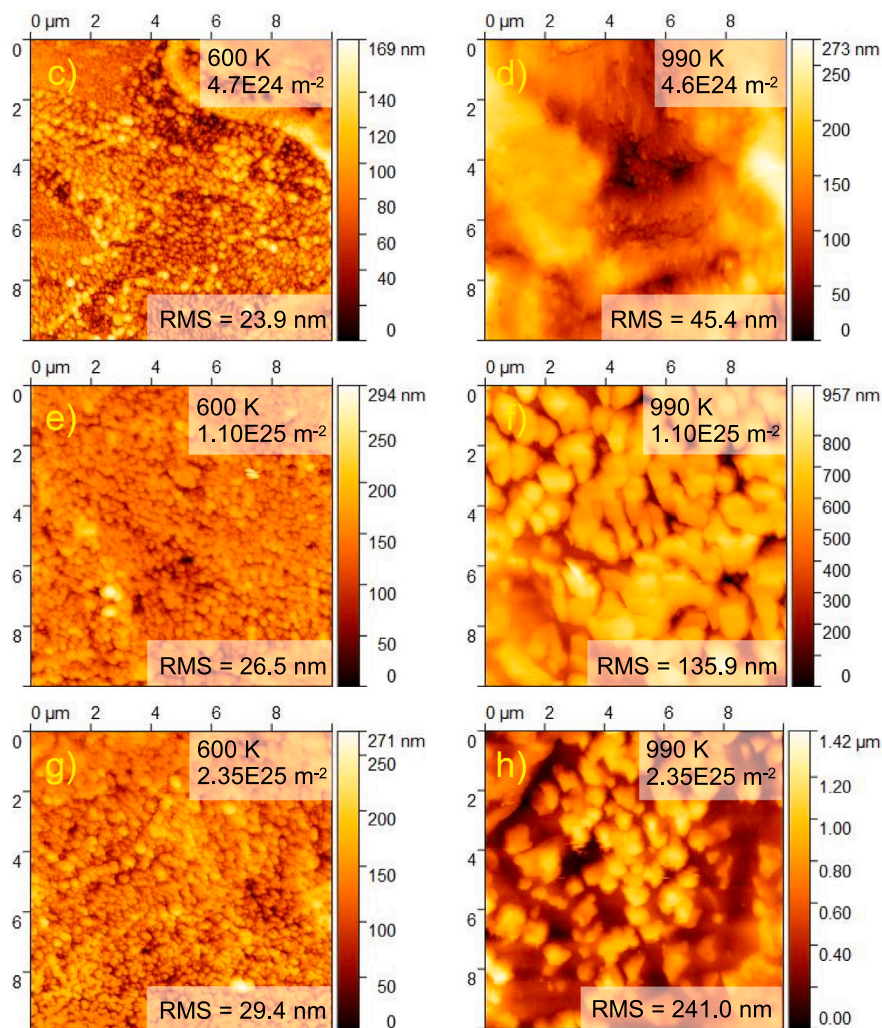


Fig. 7. 10 × 10 μm<sup>2</sup> AFM images of the surface of the same exposed samples of Fig. 6.

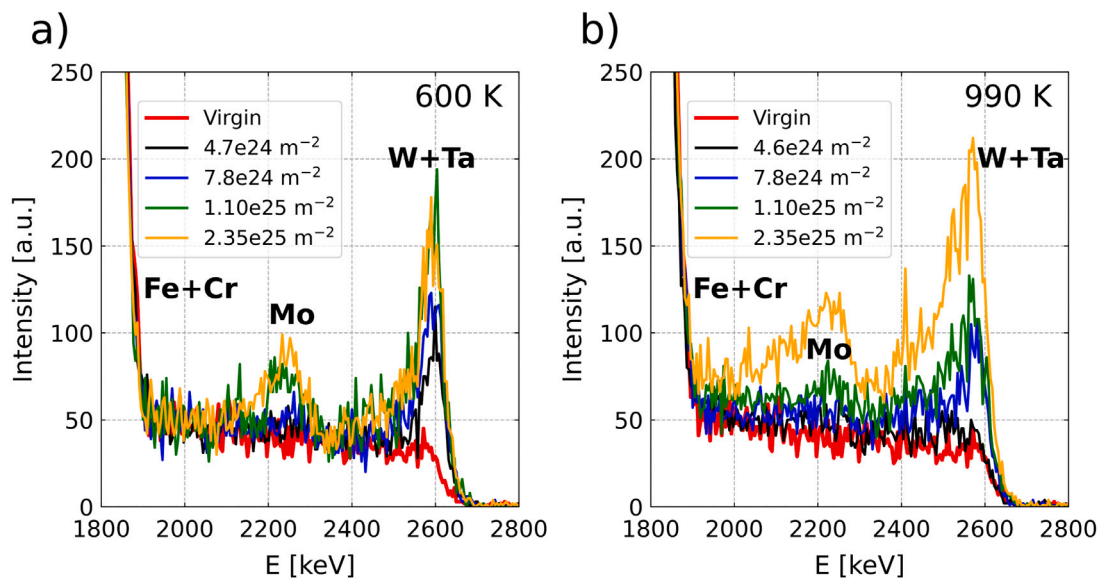


Fig. 8. RBS spectra of pristine and exposed Eurofer-97 samples at 600 K (a) and 990 K (b).

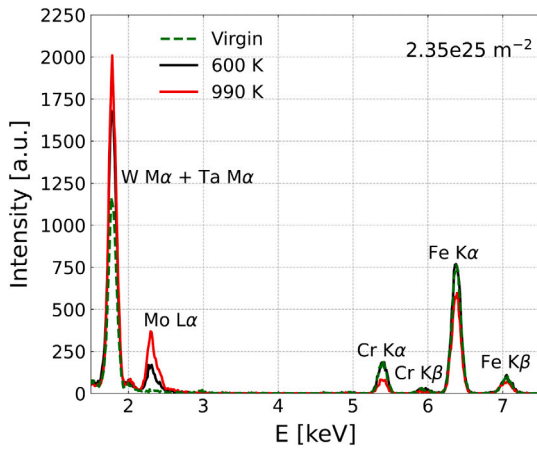


Fig. 9. PIXE spectra of virgin (dashed green line) and exposed Eurofer-97 samples at 600 K (solid black line) and 990 K (solid red line), for  $\Phi = 2.35 \times 10^{25} \text{ m}^{-2}$ . (For interpretation of the references to colour in this figure legend, the reader is referred to the web version of this article.)

height) and surface density progressively increased without reaching a steady-state at 990 K (Figs. 4a–d and 7d, f, h). This explains why the RMS roughness of Figs. 6a and 7 is almost constant at 600 K and it depends quasi-linearly on  $\Phi$  at 990 K. As far as the higher fluences are concerned, the same “asymptotic” behaviour was found for W(+Ta) enrichment from RBS and ToF-SIMS (Figs. 10a and b). It can therefore be concluded that the features of the developing morphology (size, surface density and coverage of the surface) and the amount of W(+Ta) in the surface and subsurface layers of the exposed Eurofer-97 samples are tightly linked.

The relative trends of the W(+Ta) amount from RBS and ToF-SIMS as a function of  $\Phi < 2.35 \times 10^{25} \text{ m}^{-2}$ , at the two  $T$ , can be understood in terms of the coverage of the surface by the FC morphology. As one can see from the SEM low-magnification images of Figs. 3a–d and 4a–d (left columns), almost full coverage of the surface was obtained at the lowest and the highest ion fluence for  $T = 600 \text{ K}$  and  $990 \text{ K}$ , respectively. For this reason, the W(+Ta) amount from RBS and ToF-SIMS is lower at 990 K for  $\Phi \leq 1.10 \times 10^{25} \text{ m}^{-2}$ . The turnover at the highest  $\Phi$  can be explained as follows. Coverage of the surface by the FC morphology is almost complete but there are important differences at the two temperatures if one considers the SEM high-magnification images of Figs. 3d and 4d (right columns). Specifically, surface density and lateral size of the nanostructures are factors of  $\sim 2$  higher and  $\sim 3$  lower at 600 K. Moreover, AFM and SEM tilted images of Figs. 6g–h, 7g–h and 5 show that the nanostructures’ height is by far higher at 990 K. On the whole, the total surface area of the W(+Ta) and Mo enriched FC morphology at 990 K is  $\sim 50\%$  more than that at 600 K, as computed from the  $10 \times 10 \mu\text{m}^2$  AFM images 7g–h, thus unfolding the increase of W(+Ta) amount from RBS and ToF-SIMS with the temperature at the highest ion fluence.

A higher W(+Ta) enrichment at  $2.35 \times 10^{25} \text{ m}^{-2}$  increasing the temperature is consistent with the literature of RAFM steels exposed in high-flux linear plasma devices at the same  $T$  range for fluences of  $10^{26}$ – $10^{27} \text{ m}^{-2}$  [4,8]. In particular, unlike [8], it was possible to study, in this work, the effect of the morphology on the interpretation of RBS data since the amount of W on the surface of the samples came entirely from the Eurofer-97 itself. Indeed, GyM has an AISI 304L stainless steel vessel and the  $\mu$ -wave source is electrodeless. Moreover, at  $n_e = 5.0 \times 10^{16} \text{ m}^{-3}$  and  $T_e = 7 \text{ eV}$  of the deuterium plasma of GyM, the MFP of the electron impact ionisation of W atoms is  $\sim 50 \text{ cm}$ , while the electrostatic sheath thickness near the exposed surface of the samples is a few hundred  $\mu\text{m}$  (the Debye length is  $\sim 100 \mu\text{m}$ ). Re-deposition of sputtered tungsten particles is therefore negligible.

Both the formation of the FC morphology and W(+Ta) and Mo enrichment affect the erosion rate of Eurofer-97 samples (Fig. 12). At 600 K, the initial decrease of the erosion rate followed by a steady-state behaviour can be explained by preferential sputtering of mid-Z elements [1,3]. Due to the much lower sputtering yield of high-Z elements, i.e. W, Ta and Mo, surface and subsurface regions of the samples were enriched by these elements and depleted of mid-Z elements. This led to the reduction of the erosion rate in the range of fluences up to  $8.0 \times 10^{24} \text{ m}^{-2}$ . A dynamic steady-state of the surface was then reached at higher  $\Phi$ . The qualitative behaviour of the erosion rate at 600 K should not have been influenced by the FC morphology instead, since it did not substantially evolve increasing the ion fluence (Fig. 3a–d).

At 990 K, it is worth to consider what happened below the highest  $\Phi$ , first. The higher erosion rate in this range of fluences by increasing the temperature is consistent with the lower W(+Ta) and Mo enrichment (Figs. 10a and b) of the surface of the samples due to the lower coverage by and density of the nanostructures (Fig. 4a–c, left and right columns, respectively). The almost full coverage of the surface by the nanostructures at 990 K (Fig. 4d, left column) led to the slight decrease of the erosion rate at the maximum ion fluence. Nevertheless, it is still higher than that at 600 K. The W(+Ta) and Mo amount is also higher by increasing the temperature. It is important to note at this point that the electrostatic sheath thickness near the exposed surface of the samples of a few hundred  $\mu\text{m}$  was much larger than the nanostructures’ height of  $\leq 1.5 \mu\text{m}$  (see the labels of the colorbar of AFM images 7c–h). As a result, the sheath did not follow the shape of the surface. Deuterium ions thus impinged on the rough surface parallel to the average surface normal. In view of all this, we speculate that the erosion rate can be correlated to the projected rather than the total surface area of the FC morphology. In particular, the higher the W(+Ta) and Mo enriched nanostructures projected surface area is, the lower the erosion rate. As stated previously, nanostructures coverage is almost complete at both the  $T$  for the highest  $\Phi$  (Figs. 3d and 4d, left columns). However, since nanostructures surface density is lower at 990 K, the erosion rate is higher at the highest  $T$ .

The increase of Eurofer-97 erosion rate with the temperature is consistent with the literature of RAFM steels exposed in high-flux linear plasma devices to a deuterium ion fluence  $\Phi \geq 10^{26} \text{ m}^{-2}$  [4,8].

It is now important to linger on the issue of the molybdenum deposition on the surface of the Eurofer-97 samples. Looking at the sketch of GyM sample holder of Fig. 13a, we speculate that the source of molybdenum was the side surface of the cover (highlighted in red in the picture). As a matter of fact, the small fraction of the deuterium ions impinging on this region of the holder due to the action of the magnetic pre-sheath and the electrostatic sheath (the ions trajectories are schematically represented by the red arrows), led to the sputtering of Mo atoms which could finally deposit on the Eurofer-97 sample surface. In order to test this hypothesis, Mo contamination was measured by RBS very close to the lower edge of the Mo cover (see the red spot of Fig. 13b), for the Eurofer-97 sample exposed at 600 K and  $1.10 \times 10^{25} \text{ m}^{-2}$ . Mo areal density was  $\sim 40\%$  higher than that measured at the centre of the specimen where the data of Fig. 10a were collected (see the blue spot of Fig. 13b), as expected.

We do not believe that the sputtering of the front of the cover and the strip for profilometry could be the main contributor to the Mo contamination of Eurofer-97 samples, instead. Mo MFPs for the different ionisation reactions are of the same order of magnitude of the characteristic dimensions of the experiment, i.e. GyM vacuum vessel diameter of 0.25 m and the 1 m distance between the sample holder and the cylinder base in front of it, due to the fairly low GyM plasma density. As discussed in Section 2, the MFP for electron impact ionisation is  $\sim 0.4 \text{ m}$  (for  $n_e = 5.0 \times 10^{16} \text{ m}^{-3}$  and  $T_e = 7 \text{ eV}$ ). Mo atoms sputtered from the front of cover and the strip easily escaped the few hundred  $\mu\text{m}$  thick electrostatic sheath near the sample holder first and then had a great chance to reach the wall still as neutrals. The small fraction of Mo atoms being ionised by electron impact, mostly followed



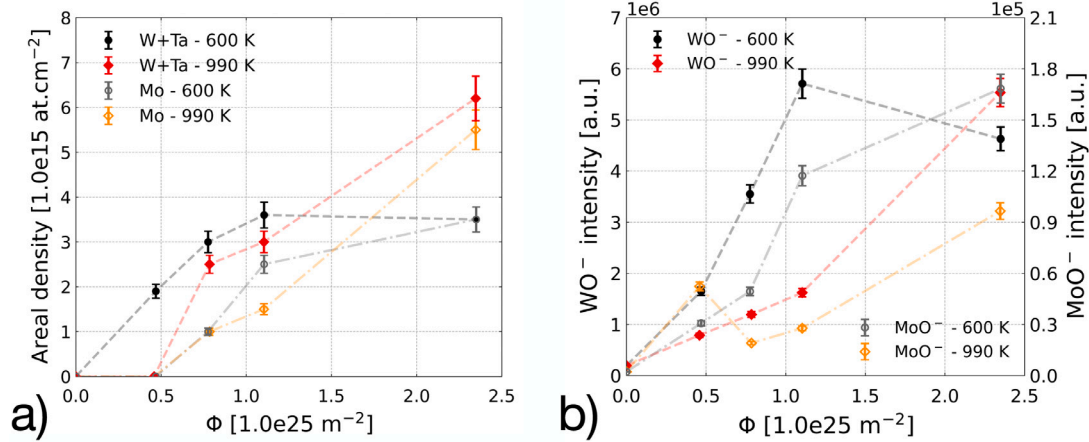


Fig. 10. (a) W+Ta and Mo areal densities, estimated from RBS, and (b) ToF-SIMS depth profiling  $\text{WO}^-$  and  $\text{MoO}^-$  integrated signals as a function of ion fluence at 600 K (filled black and open grey circles) and 990 K (filled red and open orange diamonds). Dashed lines are drawn to guide the eye. (For interpretation of the references to colour in this figure legend, the reader is referred to the web version of this article.)

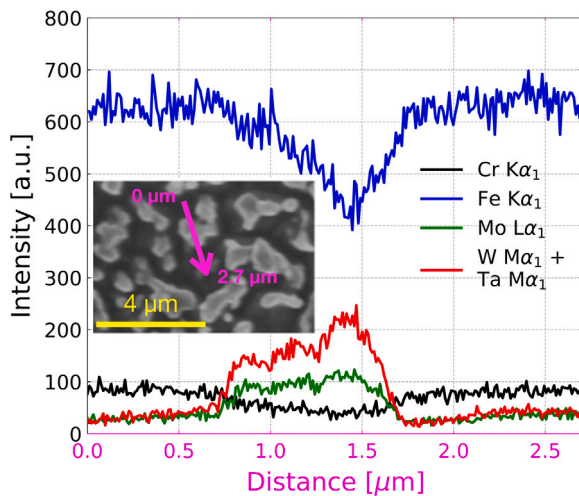


Fig. 11. EDX line-scan analysis along the 2.7  $\mu\text{m}$  magenta arrow painted on the SEM image shown in inset, for the sample exposed at the highest  $\Phi$  and 990 K.

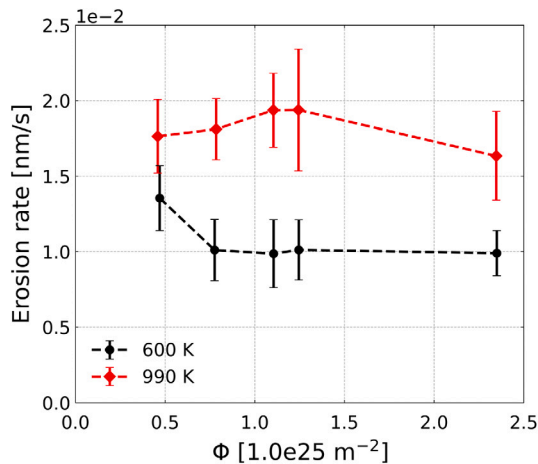


Fig. 12. Erosion rate of Eurofer-97 samples, evaluated from profilometry measurements, as a function of the ion fluence for the experiments at 600 K (filled black circles) and 990 K (filled red diamonds). Each scatter point is the average of the twenty-one independent measurements of the eroded step divided by the exposure time, and the error bar represents the associated standard deviation. Dashed lines are drawn to guide the eye. (For interpretation of the references to colour in this figure legend, the reader is referred to the web version of this article.)

the magnetic field lines ending on the cylinder base. The probability for the Mo atoms on the wall to be re-sputtered by deuterium ions and eventually come back to the sample-holder was low since GyM vacuum vessel was electrically grounded.

Once the sputtered Mo atoms coming in line of sight from the side of the cover reached the surface of the exposed sample, we infer that they behaved like the atoms of the main high-Z elements of the alloy, tungsten and tantalum, since Mo is also a high-Z element and its chemistry is similar to that of W. EDXS showed indeed that Mo mainly concentrated in the nanostructures, together with W and Ta (Fig. 11). Moreover, the trends of Mo and W(+Ta) amount as a function of  $\Phi$ , at the two T, from RBS and ToF-SIMS resemble each other (Figs. 10a and b). We conclude that the presence of Mo on the surface of the samples does not substantially affect the interpretation of the results of the exposures given in this Section.

Mo contamination detected by RBS and ToF-SIMS at the region protected by the Mo strip for profilometry could be explained again by the deposition of Mo atoms sputtered from the side surface of the cover, if the strip did not adhere well to the specimen. In the regions where the adhesion between the sample and the strip was good, Mo impurities could come instead from the contact at high temperature with the Mo strip. The presence of contaminants at the protected surface was also supported by SEM images (e) of Figs. 3 and 4.

From the point of view of the topic of plasma-wall interaction in tokamaks, it is important to stress again that GyM ion flux of  $10^{20}$ – $10^{21}$   $\text{m}^{-2}\text{s}^{-1}$  is pretty close to the expected CXNs flux impinging on the recessed elements of the DEMO first-wall [18]. This is particularly relevant to properly predict the behaviour of these components since plasma interaction effects on their properties, as surface composition and erosion, may be flux-dependent [5,20]. Moreover, the range of deuterium ion fluences  $\Phi = 10^{24}$ – $10^{25}$   $\text{m}^{-2}$  investigated here, unlike the values of  $\Phi \geq 10^{26}$   $\text{m}^{-2}$  considered in [4,8], enabled to study plasma-material interaction during the first hours of operation. If Eurofer-97 will be chosen for DEMO first-wall recessed components, their erosion rate will decrease with time (i.e., increasing hydrogen isotope CXNs fluence) as a consequence of the mid-Z steel elements preferential sputtering, reaching a steady-state value after few hours, for stable plasma conditions.

As mentioned above, this work agrees with [4,8] that Eurofer-97 erosion rate increases with T. DEMO transient events which could potentially bring the temperature of first-wall recessed elements above the allowed upper limit of 823 K [19], would increase their erosion rate as well as lead to the degradation of their mechanical properties. They should therefore be avoided or at least strongly mitigated.

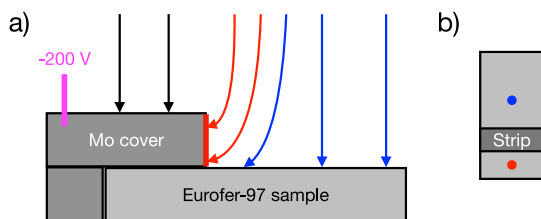


**Fig. 13.** (a) Schematic of the incidence angle of incoming ion trajectories on GyM sample holder (drawing not to scale). The bias voltage applied to both the specimen and the sample holder was  $-200$  V. (b) Sketch of Eurofer-97 specimen exposed in GyM. RBS data of Fig. 10a were collected at the blue spot. For the sample exposed at 600 K and  $1.10 \times 10^{25} \text{ m}^{-2}$ , further RBS data were collected at the red spot to test the hypothesis that the side surface of the cover was the source of Mo contamination. (For interpretation of the references to colour in this figure legend, the reader is referred to the web version of this article.)

Molybdenum contamination of Eurofer-97 surface during the deuterium plasma exposure in GyM makes the experiments more DEMO-relevant in a sense. Indeed, Mo and other high-Z elements like rhodium are, for example, among the candidates for the manufacturing of future reactors optical diagnostics first mirrors [28,29] that will be subject to plasma erosion. The sputtered particles could migrate into the scrape-off layer and eventually deposit on the other components of the first-wall.

## 5. Conclusions

Eight mirror finished Eurofer-97 samples were exposed to the deuterium plasma of the linear device GyM, whose ion flux of  $10^{20}$ – $10^{21} \text{ m}^{-2} \text{ s}^{-1}$  is suitable to simulate the hydrogen isotope charge-exchange neutrals (CXNs) flux impinging on the recessed components of the DEMO first-wall. A bias voltage of  $-200$  V was applied to GyM sample holder to obtain typical CXNs low energies. Eurofer-97 erosion dynamics was investigated at sample temperatures  $T$  of 600 K and 990 K, for different deuterium ion fluences in the range  $\Phi = 4.6 \times 10^{24}$ – $2.35 \times 10^{25} \text{ m}^{-2}$ . Sample erosion rates were evaluated by profilometry. The evolution of morphology and roughness were studied by scanning electron microscopy and atomic force microscopy. Compositional changes were investigated by energy-dispersive X-ray spectroscopy, time-of-flight secondary ion mass spectrometry, Rutherford backscattering spectroscopy and particle-induced X-ray emission. The main findings can be schematically drawn as follows:

1. A fence/corral-like (FC) morphology [8] with nanostructures enriched by tungsten (W), tantalum (Ta) and molybdenum (Mo), the latter coming from the sputtering of the sample holder, developed on the surface of Eurofer-97 samples at the end of the experiments.
2. The comparison of the results of microscopy and surface analysis techniques revealed that the features of the FC morphology (size, surface density and coverage of the surface) and the amount of W(+Ta) in the surface and subsurface layers are tightly linked. The reason for this can be attributed to the synergistic effect of a multitude of processes [4,6,8,10]: preferential sputtering of iron and other mid-Z elements of Eurofer-97, the radiation-induced surface segregation, the radiation-enhanced diffusion, the deuterium-enhanced surface diffusion, the “simple” thermal surface diffusion and the nano-crystallite nucleation induced by high-Z elements, like W and Ta of the alloy but also deposited Mo.
3. Eurofer-97 erosion rate is affected by both the formation of the FC morphology and the enrichment by W(+Ta) and Mo. At 600 K, the initial decrease of the erosion rate followed by a steady-state behaviour can be explained by mid-Z elements preferential sputtering. The qualitative behaviour of the erosion

rate at 600 K should not have been influenced by the FC morphology instead, since it did not substantially evolve increasing the ion fluence. The erosion rate is higher at 990 K, for every  $\Phi$ . Below the highest  $\Phi$ , this is consistent with the lower high-Z elements, W, Ta and Mo, enrichment of the surface of the samples, as a consequence of the lower coverage of the surface by and density of the nanostructures. For the highest ion fluence, both the erosion rate and W(+Ta) and Mo amount are higher at 990 K, instead. In order to explain this, we speculate that the measured high-Z elements enrichment is correlated to the total surface area of the FC morphology which is higher at 990 K, on the one hand, and that the measured erosion rate is correlated to the projected surface area of the nanostructures which is lower at 990 K, on the other hand.

From the point of view of the topic of plasma-wall interaction in tokamaks, if Eurofer-97 will be chosen as the material for the recessed elements of the DEMO first-wall, it will be important to keep their temperature well below 990 K. In this way, the erosion rate will decrease during the operation as a consequence of the mid-Z steel elements preferential sputtering reaching a steady-state value after few hours, thus increasing the lifetime of the components.

## CRedit authorship contribution statement

**Andrea Uccello:** Investigation, Writing – original draft, Writing – review & editing, Supervision. **Francesco Ghezzi:** Investigation, Writing – original draft, Writing – review & editing. **Janez Kovač:** Investigation, Writing – review & editing. **Jernej Ekar:** Investigation. **Tatjana Filipič:** Investigation. **Iva Bogdanović Radović:** Investigation, Writing – review & editing. **David Dellasega:** Investigation, Writing – review & editing. **Vittoria Mellera:** Investigation. **Matteo Pedroni:** Investigation, Writing – review & editing. **Daria Ricci:** Investigation, Writing – review & editing.

## Declaration of competing interest

The authors declare that they have no known competing financial interests or personal relationships that could have appeared to influence the work reported in this paper.

## Data availability

Data will be made available on request.

## Acknowledgements

This work has been carried out within the framework of the EUROfusion Consortium, funded by the European Union via the Euratom Research and Training Programme (Grant Agreement No 101052200 - EUROfusion). Views and opinions expressed are however those of the author(s) only and do not necessarily reflect those of the European Union or the European Commission. Neither the European Union nor the European Commission can be held responsible for them. The activity has been performed under EUROfusion work-package plasma facing components (WP-PFC, FP8).

## References

- [1] J. Roth, K. Sugiyama, V. Alimov, T. Höschen, M. Baldwin, R. Doerner, EUROFER as wall material: Reduced sputtering yields due to W surface enrichment, *J. Nucl. Mater.* 454 (1) (2014) 1–6.
- [2] P. Ström, P. Petersson, M. Rubel, D. Primetzhofer, S. Brezinsek, A. Kreter, B. Unterberg, G. Sergienko, K. Sugiyama, Ion beam analysis of tungsten layers in EUROFER model systems and carbon plasma facing components, *Nucl. Instrum. Methods Phys. Res. Sect. B* 371 (2016) 355–359.
- [3] K. Sugiyama, M. Balden, S. Elgeti, T. Höschen, M. Oberkofler, J. Roth, W. Jacob, Erosion of EUROFER steel by mass-selected deuterium ion bombardment, *Nucl. Mater. Energy* 16 (2018) 114–122.



- [4] V. Alimov, Y. Hatano, N. Yoshida, H. Watanabe, M. Oyaidzu, M. Tokitani, T. Hayashi, Surface modification and sputtering erosion of reduced activation ferritic martensitic steel F82H exposed to low-energy, high flux deuterium plasma, *Nucl. Mater. Energy* 7 (2016) 25–32.
- [5] U. von Toussaint, A. Mutzke, K. Sugiyama, T. Schwarz-Selinger, Simulation of coupled sputter-diffusion effects, *Phys. Scr. T167* (2016) 014023.
- [6] O. Ogorodnikova, Z. Zhou, K. Sugiyama, M. Balden, Y. Gasparyan, V. Efimov, Surface modification and deuterium retention in reduced-activation steels under low-energy deuterium plasma exposure. Part I: Undamaged steels, *Nucl. Fusion* 57 (3) (2017).
- [7] R. Caniello, A. Uccello, F. Ghezzi, D. Minelli, I. Bogdanović Radović, Z. Siketić, A. Cremona, F. Dell’Era, G. Gittini, V. Meller, F. Pallotta, M. Pedroni, D. Ricci, N. Spinicchia, E. Vassallo, Erosion yield and W surface enrichment of Fe-W model system exposed to low flux deuterium plasma in the linear device GyM, *Nucl. Mater. Energy* 10 (2017) 9–16.
- [8] M. Balden, S. Elgeti, M. Zibrov, K. Bystrov, T. Morgan, Effect of the surface temperature on surface morphology, deuterium retention and erosion of EUROFER steel exposed to low-energy, high-flux deuterium plasma, *Nucl. Mater. Energy* 12 (2017) 289–296.
- [9] P. Ström, P. Petersson, R. Arredondo Parra, M. Oberkofler, T. Schwarz-Selinger, D. Primetzhofer, Sputtering of polished EUROFER97 steel: Surface structure modification and enrichment with tungsten and tantalum, *J. Nucl. Mater.* 508 (2018) 139–146.
- [10] V. Alimov, Y. Hatano, N. Yoshida, N. Bobyr, M. Oyaidzu, M. Tokitani, T. Hayashi, Surface morphology of F82H steel exposed to low-energy D plasma at elevated temperatures, *J. Nucl. Mater.* 510 (2018) 366–372.
- [11] H.R. Koslowski, S.R. Bhattacharyya, P. Hansen, Ch. Linsmeier, M. Rasiński, P. Ström, Temperature-dependent in-situ LEIS measurement of W surface enrichment by 250 eV D sputtering of EUROFER, *Nucl. Mater. Energy* 16 (2018) 181–190.
- [12] U. von Toussaint, A. Mutzke, Fluence dependent changes of erosion yields and surface morphology of the iron-tungsten model system: SDTrimSP-2D simulation studies, *Nucl. Mater. Energy* 12 (2017) 318–322, Proceedings of the 22nd International Conference on Plasma Surface Interactions 2016, 22nd PSI.
- [13] R. Arredondo, M. Balden, A. Mutzke, U. von Toussaint, S. Elgeti, T. Höschen, K. Schlueter, M. Mayer, M. Oberkofler, W. Jacob, Impact of surface enrichment and morphology on sputtering of EUROFER by deuterium, *Nucl. Mater. Energy* 23 (2020) 100749.
- [14] G. Granucci, D. Ricci, S. Alocci, B. Baiocchi, W. Bin, A. Bruschi, A. Cremona, O. D’Arcangelo, M. De Angeli, F. Dell’Era, F. Gandini, S. Garavaglia, G. Gatto, G. Gervasini, G. Gittini, G. Grossetti, G. Grosso, E. Lazzaro, M. Lontano, V. Meller, V. Muzzini, A. Moro, A. Nardone, R. Schiavone, N. Spinicchia, C. Sozzi, The new linear plasma device GyM at IFP-CNR, in: Proceeding of the 36th EPS Conference, June 29 - July 3 2009, Sofia, Bulgaria, ECA, Vol. 33E, 2009, P-4.148.
- [15] D. Ricci, A. Cremona, S. Garavaglia, G. Granucci, S. Alocci, M. DeAngeli, F. Dell’Era, G. Gatto, G. Gervasini, G. Gittini, M. Lontano, V. Meller, D. Minelli, V. Muzzini, A. Nardone, R. Schiavone, C. Sozzi, Characterization of electrostatic fluctuations in the low-density plasma of the linear device GyM, in: 37th EPS Conference on Plasma Physics 2010, EPS 2010, Vol. 1, 2010, pp. 517–520.
- [16] A. Uccello, F. Ghezzi, L. Laguardia, R. Caniello, D. Dellasega, F. dell’Era, D. Della Torre, R. Donnini, G. Granucci, E. Mesto, D. Minelli, M. Passoni, M. Pedroni, A. Pezzoli, D. Ricci, Effects of a nitrogen seeded plasma on nanostructured tungsten films having fusion-relevant features, *Nucl. Mater. Energy* 25 (2020) 100808.
- [17] A. Uccello, W. Bin, A. Bruschi, F. Causa, A. Cremona, M. De Angeli, D. Farina, G. Gatto, G. Gervasini, F. Ghezzi, G. Gittini, G. Granucci, G. Grosso, L. Laguardia, M. Lontano, V. Meller, D. Minelli, A. Nardone, M. Pedroni, F. Ripamonti, N. Rispoli, E. Vassallo, D. Ricci, Linear plasma device GyM for plasma-material interaction studies, *Front. Phys.* 11 (2023) <http://dx.doi.org/10.3389/fphy.2023.1108175>.
- [18] H. Bolt, V. Barabash, G. Federici, J. Linke, A. Loarte, J. Roth, K. Sato, Plasma facing and high heat flux materials - needs for ITER and beyond, *J. Nucl. Mater.* 307–311 (2002) 43–52.
- [19] Yu. Igitkhanov, R. Fetzer, B. Bazylev, Effect of design geometry of the demo first wall on the plasma heat load, *Nucl. Mater. Energy* 9 (2016) 560–564.
- [20] R.P. Doerner, Sputtering in a high-flux plasma environment, *Scr. Mater.* 143 (2018) 137–141.
- [21] R. Lindau, A. Möslang, M. Rieth, M. Klimiankou, E. Materna-Morris, A. Alamo, A.-A.F. Tavassoli, C. Cayron, A.-M. Lancha, P. Fernandez, N. Baluc, R. Schäublin, E. Diegele, G. Filacchioni, J.W. Rensman, B. v. d. Schaaf, E. Lucon, W. Dietz, Present development status of EUROFER and ODS-EUROFER for application in blanket concepts, *Fusion Eng. Des.* 75–79 (2005) 989–996, Proceedings of the 23rd Symposium of Fusion Technology.
- [22] K. Sugiyama, K. Schmid, W. Jacob, Sputtering of iron, chromium and tungsten by energetic deuterium ion bombardment, *Nucl. Mater. Energy* 8 (Supplement C) (2016) 1–7.
- [23] A. Eksaeva, E. Marenkov, D. Borodin, A. Kreter, M. Reinhart, A. Kirschner, J. Romazanov, A. Terra, S. Brezinsek, K. Nordlund, ERO modelling of tungsten erosion in the linear plasma device PSI-2, *Nucl. Mater. Energy* 12 (2017) 253–260, Proceedings of the 22nd International Conference on Plasma Surface Interactions 2016, 22nd PSI.
- [24] M. Mayer, SIMNRA User’s Guide, Report IPP 9/113, Max-Planck-Institut für Plasmaphysik, Garching, Germany, 1997.
- [25] W. Eckstein, M. Mayer, Rutherford backscattering from layered structures beyond the single scattering model, *Nucl. Instrum. Methods Phys. Res. Sect. B* 153 (1–4) (1999) 337–344.
- [26] J. Ekar, P. Panjan, S. Drev, J. Kovač, ToF-SIMS depth profiling of metal, metal oxide, and alloy multilayers in atmospheres of H<sub>2</sub>, C<sub>2</sub>H<sub>2</sub>, CO, and O<sub>2</sub>, *J. Am. Soc. Mass Spectrom.* 33 (1) (2022) 31–44.
- [27] W.S. Rasband, ImageJ, U. S. National Institutes of health, Bethesda, Maryland, USA, 1997-2018, URL <https://imagej.nih.gov/ij/>.
- [28] M. Joanny, J.M. Travère, S. Salasca, Y. Corre, L. Marot, C. Thellier, G. Gally, C. Cammarata, B. Passier, J.J. Fermé, Engineering and manufacturing of ITER first mirror mock-ups, *Rev. Sci. Instrum.* 81 (10) (2010) 10E108.
- [29] M. Rubel, Sunwoo Moon, P. Petersson, A. Widdowson, R.A. Pitts, S. Aleiferis, E. Fortuna-Zalešna, G. De Temmerman, R. Reichle, First mirror erosion-deposition studies in JET using an ITER-like mirror test assembly, *Nucl. Fusion* 61 (4) (2021) 046022.